Structure formation on the surface of indium phosphide irradiated by femtosecond laser pulses

J. Bonse[a)]
Instituto de Optica, Consejo Superior de Investigaciones Cientificas (CSIC), Serrano 121, E-28006 Madrid, Spain

M. Munz and H. Sturm
Fachgruppe VI.2: Mechanik der Polymere und Faserverbundwerkstoffe, Bundesanstalt für Materialforschung und -prüfung (BAM), Unter den Eichen 87, D-12205 Berlin, Germany

(Received 20 May 2004; accepted 8 October 2004; published online 16 December 2004)

Laser-induced periodic surface structures (LIPSS; ripples) with different spatial characteristics have been observed after irradiation of single-crystalline indium phosphide (*c*-InP) with multiple linearly polarized femtosecond pulses (130 fs, 800 nm) in air. With an increasing number of pulses per spot, *N*, up to 100, a characteristic evolution of two different types of ripples has been observed, i.e., (i) the growth of a grating perpendicular to the polarization vector consisting of nearly wavelength-sized periodic lines and (ii), in a specific pulse number regime ($N=5-30$), the additional formation of equally oriented ripples with a spatial period close to half of the laser wavelength. For pulse numbers higher than 50, the formation of micrometer-spaced grooves has been found, which are oriented perpendicular to the ripples. These topographical surface alterations are discussed in the frame of existing LIPSS theories. © *2005 American Institute of Physics*. [DOI: 10.1063/1.1827919]

I. INTRODUCTION

Since the observation of *laser-induced periodic surface structures* (LIPSS), also termed as *ripples*, on semiconductors by Birnbaum,[1] those structures have been observed on almost every material. The generation of ripples upon laser irradiation is a universal phenomenon,[2–4] even if the exact physical mechanism and their occurrence can depend on the irradiated material and the irradiation parameters.

In many cases, after exposure to linearly polarized radiation at normal incidence, the lateral period of the observed surface structures is very close to the wavelength of the incident radiation. It is generally accepted that this type of *wavelength ripple* arises from optical interference effects due to the superposition of the incident radiation with a surface-electromagnetic wave which is created at the rough surface during the irradiation and which is scattered along the surface.[2,4–6]

With respect to the irradiation with femtosecond laser pulses, ripples with spatial periods close to the wavelength λ have been reported on various absorbing materials such as metals,[7] ceramics,[8,9] and semiconductors.[10–13] Interestingly, in most of these cases the ripple period is somewhat smaller than the wavelength and their orientation is mostly perpendicular to the electric-field vector. These nearly wavelength-sized ripples have been mainly observed for moderate pulse numbers (*N* smaller than ~ 100) at fluences slightly above the single-pulse ablation threshold of the material.

In very recent studies of the femtosecond laser ablation, new types of *subwavelength ripples* with periods as small as $\lambda/6$ in some cases have been reported by various groups upon irradiation of very different materials with hundreds to thousands of pulses per spot and at fluences *below* the single-pulse ablation threshold.[8,13–15] The nature of those subwavelength ripples is still quite controversially discussed in the literature.

For the III-V semiconducting compound material indium phosphide (InP), the wavelength-sized ripples have been observed for the irradiation with linearly polarized Ti:sapphire laser radiation (800 nm, 130 fs pulse duration) having an orientation of the periodic lines perpendicular to the incident electric-field vector.[11] Very recently, the formation of subwavelength-sized ripples has been reported by Borowiec and Haugen for the irradiation of various compound semiconductors, including InP by 50–130 fs laser pulses at several wavelengths (800, 1300, and 2100 nm) and for typically between 1 and 100 pulses per spot.[14] Near the ablation threshold, these authors reported the formation of *high-spatial-frequency LIPSS* (HSFL), with lateral periods 4.2–5.1 times smaller than the wavelength of the incident light, only when the laser photon energy is below the band-gap energy of the target materials. "Classical" *low-spatial-frequency LIPSS* (LSFL), with a spatial period close to the wavelength of the excitation pulse, were observed on all investigated materials and for all wavelengths.[14] Both types of ripples (HSFL and LSFL) were always oriented perpendicular to the electric-field vector of the linearly polarized femtosecond laser radiation.

In this work, we present a complementary study on the formation of LIPSS in InP after above-band-gap excitation with near-infrared femtosecond laser pulses, including a detailed analysis of the influence of the number of pulses per spot. This study extends the work performed at the Ti:sapphire laser irradiation at 800 nm, namely, a new type of

[a)]Author to whom correspondence should be addressed; electronic mail: jbonse@io.cfmac.csic.es

ripples with a spatial period close to half of the laser wavelength was observed. Moreover, characteristic micrometer-sized grooves were found to form under specific irradiation conditions. A comparison of these experimental results with the currently accepted theory on LIPSS reveals that the observed surface structures can be explained only partly by the existing theories.

II. EXPERIMENT

A commercial chirped-pulse amplification-based Ti:sapphire regenerative amplifier (Spectra Physics, Spitfire) was used to generate linearly polarized laser pulses at a wavelength of $\lambda = 800$ nm and with a pulse duration of $\tau = 130$ fs. An electromechanical shutter selected a desired number of laser pulses (N between 1 and 100) from a pulse train of 10 Hz repetition frequency. At this repetition rate, heat dissipation between the laser pulses was sufficient to prevent changes in the initial temperature of the wafer during repetitive illumination. Using a 60 mm focal distance lens, the laser pulses were focused directly onto the surface of an *n*-doped (100) indium phosphide wafer (American Xtal technologies). The central part of the laser focus was approximated by a Gaussian intensity distribution with a radius of $w_0 = 23$ μm (as measured at $1/e^2$ of the maximum intensity). The laser fluence of the incident light was varied by using a combination of a half-wave plate and a linear polarizer. A pyroelectric detector was used to measure the laser-pulse energy. A motorized *xyz* stage allowed the precise positioning of the wafer between the irradiation sequences. All irradiations were performed in air. Further details of the sample irradiation conditions can be found in Ref. 11.

The ablation morphologies were characterized by means of a scanning force microscope (SFM; type "Explorer," ThermoMicroscopes/TopoMetrix, Santa Clara, USA) which allows quantitative measurements with both a high lateral and vertical precision in the nanometer range. Since the operational regime of this SFM is restricted to a small crater depth, the investigation of surface regions irradiated with a large number of laser pulses was made by means of a scanning electron microscope (SEM) equipped with a cold-field electron emission cathode (Hitachi, S-4001, accelerating voltage of 10 kV).

III. RESULTS AND DISCUSSION

In order to investigate the evolution of morphological changes under the action of femtosecond laser pulses, several identical pulses ($N = 1-100$) were applied to the same location on the InP sample at fluence values approximately 1–3 times the threshold fluence for single-pulse ablation [$\phi_{abl}(1) = 0.23$ J/cm^2, Ref. 16]. Besides the *crater formation*, various pulse-number-dependent surface structures, such as periodic *ripples*, micrometer-sized *cones*, and characteristic micrometer-sized *grooves*, were observed. The results of their characterization are described in detail in the following sections. Since a more detailed SFM study of the cone structures has been already published in Ref. 17, those structures will not be discussed here in great detail.

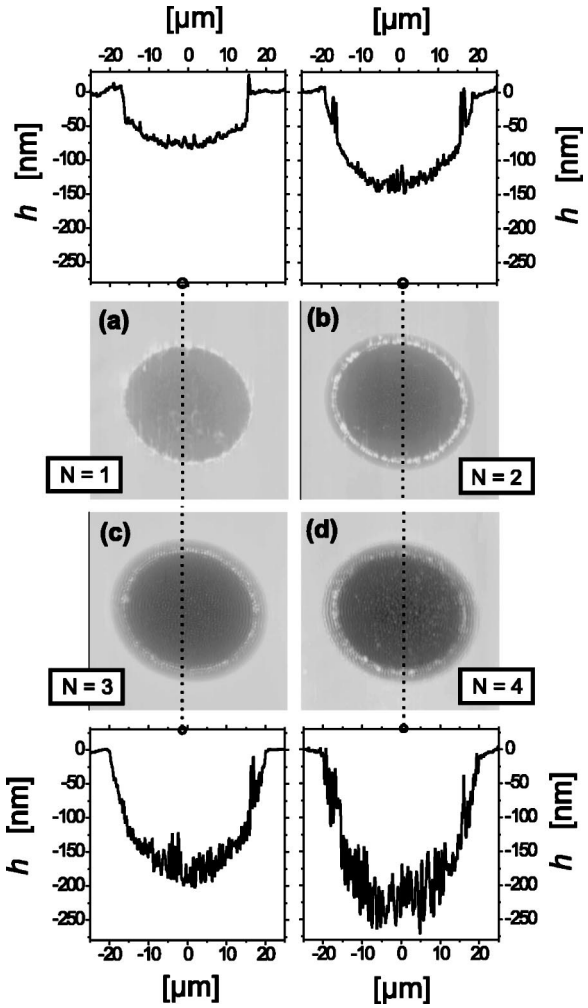

FIG. 1. SFM topography (50×50 μm^2) of craters in InP processed by different numbers of laser pulses applied to the same spot: (a) $N=1$, (b) $N=2$, (c) $N=3$, and (d) $N=4$ ($\phi_0 = 0.58$ J/cm^2, 800 nm, 130 fs). Additionally, cross-sectional views along the dashed vertical lines are given. In each case, the upper end of the dashed line corresponds to the left-handed side of the corresponding cross-sectional profile. All the topography images are encoded by the same gray scale.

A. Crater formation

SFM measurements were performed at a series of craters generated at a peak fluence of $\phi_0 = 0.58$ J/cm^2 in order to investigate quantitatively the changes in the ablation morphologies induced by multiple-laser-pulse ablation. The change of the surface topography with an increasing number of laser pulses applied to the same spot ($N = 1-4$) is shown in Fig. 1. Additionally, cross sections along the dashed lines are displayed for each image.

The action of a single laser pulse ($N=1$) leads to the formation of an approximately 80-nm-deep crater exhibiting a roughened and featureless bottom and steep crater walls [Fig. 1(a)]. This demonstrates that a very precise material removal is possible for the femtosecond laser-pulse ablation of InP. At the edge of the crater a protruding rim (height of <20 nm, width of ~ 300 nm) is formed [Fig. 1(a)], which most likely arises from the recoil pressure of the ablating material. One additional laser pulse ($N=2$) generates a double structure of the rim, possibly caused by small fluc-

tuations in the laser energy of the second pulse [Fig. 1(b)]. Interestingly, ablation takes place also outside the rim structure. This can be explained by two different effects: (1) Outside the ablated region there exists an annular zone where the surface material has been transferred into an amorphous state (*a*-InP) under the action of the first laser pulse (melting without ablation).[16] Hence, a thin top layer with altered thermal and optical properties has formed which is not obvious from the SFM topography. The penetration depth of light at the laser processing wavelength of 800 nm is reduced by a factor of more than 2 [$1/\alpha$(*c*-InP)=310 nm and $1/\alpha$(*a*-InP) =140 nm; the linear absorption coefficient α is taken from Refs. 18 and 19 respectively]. Thus, even when neglecting nonlinear effects at high intensities or free-carrier absorption in the modified material, the depth of energy deposition is reduced, leading to an increased energy localization in the amorphous top layer and consequently to the ablation of the material outside the rim formed by the first laser pulse. (2) Additionally, the material in the border region of the crater is mechanically stressed, as shown by micro-Raman spectroscopy.[16] The stressed material can exhibit reduced threshold fluences for melting and ablation.[20]

With increasing number of pulses, small protruding caps develop at the bottom of the crater [Fig. 1(b)]. These caps are even more pronounced in the central part of the crater after the application of three subsequent pulses [$N=3$, Fig. 1(c)]. In the outer regions of the ablated area a periodic ripple structure develops [Figs. 1(c) and 1(d)].

B. Ripple formation

In order to investigate the periodic structures within the ablated areas in more detail, the images shown in Fig. 1 were subjected to a discrete two-dimensional Fourier transformation (2D-FT), using the image processing software SPIP 2.004 (Image Metrology A/S, Lyngby, Denmark). The corresponding Fourier transformed images are displayed in Fig. 2.

The central regions of Figs. 2(a)–2(d) reflect large spatial frequencies (i.e., large-scale corrugations like the crater itself), whereas the border region is determined by the spatial pixel resolution of the SFM images (100 nm). The dark regions represent increased amplitudes in the Fourier space. It is interesting to note that after the first laser pulse, essentially no spatial frequencies in the order of the laser wavelength are visible [Fig. 2(a)]. But after the second laser pulse per spot, some periodical surface features of these lateral periods are already present [Figs. 2(b)–2(d)]. The 2D-FT image is then dominated by two sickle-shaped features associated with the periodic ripple pattern. The corresponding spatial frequencies are around $\Lambda \sim \pm 750$ nm, with an absolute value close to the femtosecond laser processing wavelength $\lambda = 800$ nm. Hence, one can conclude that the first laser pulse generates a roughened surface leading to some scattering of the subsequent laser pulses.

From the fact that the spatial periods of the ripples nearly coincide with the laser radiation wavelength ($|\Lambda| \approx \lambda$) while their orientation favors the direction perpendicular to the polarization of the incident laser radiation, the phenomenon can be attributed to the well-known mechanism of

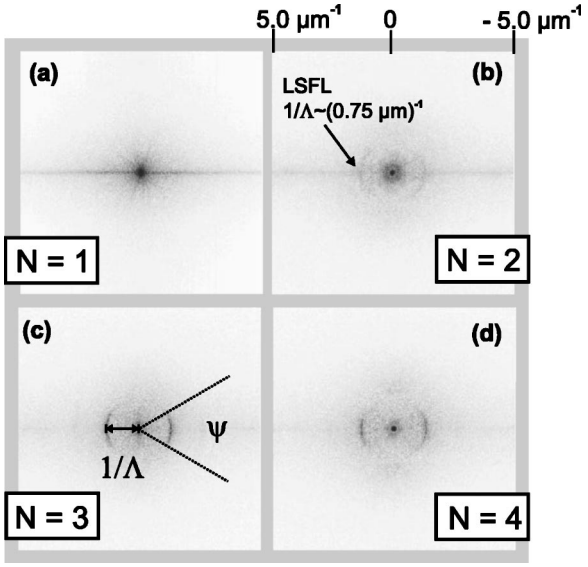

FIG. 2. Results of the two-dimensional Fourier transformation of the four SFM topography images shown in Fig. 1. (a) $N=1$, (b) $N=2$, (c) $N=3$, and (d) $N=4$ ($\phi_0=0.58$ J/cm^2, 800 nm, 130 fs). The Fourier amplitudes are encoded in a linear gray scale, with the dark regions representing the high values. In (c), the opening angle ψ of the sickle-shaped LSFL feature is indicated.

scattering/diffraction and subsequent local-field enhancement via interference.[4,6] The interference between the incident linearly polarized light and a surface wave (generated by scattering during the pulse) leads to a periodic modulation of the absorbed light intensity and consequently to a modulated ablation, which enhances the development of the structure via feedback. In analogy to Ref. 14, this ripple-type is referred to as LSFL.

Cross sections through the border regions of the craters depicted in Fig. 1 (not shown here) reveal that the wavelength-sized ripples have a modulation depth in the order of 100 nm, which is in good agreement with a previous study.[17] Complementary cross-sectional transmission electron microscopy studies by Borowiec *et al.* evidence that the ripples (modulation depths of ~200 nm at similar fluences of ~0.7 J/cm^2) consist, at least partly, of resolidified material.[12]

In order to investigate quantitatively the influence of the number of pulses in the entire range between single and 100 pulses per spot, the SEM images with a fixed area of 41.3 $\times$ 41.3 μm^2 were subjected to a 2D-FT analysis (pixel resolution of ~83 nm). Figure 3 shows the evolution of the characteristic parameters obtained from this pulse number variation series ($\phi_0=0.58$ J/cm^2, 800 nm, 130 fs), i.e., (a) the spatial period Λ of the ripples, (b) the opening angle ψ [as indicated in Fig. 2(c)], and (c) the maximum frequency with which the wavelength ripples were detected. Some typical corresponding 2D-FT images and SEM details are given in (d).

It is evident from Fig. 3(a) that the average ripple period of the LSFL monotonously decreases from an initial value close to the wavelength ($\Lambda \sim 750$ nm for $N=2$) to significantly smaller values ($\Lambda \sim 590$ nm for $N=100$). Along with this, the variation of this ripple period around its average

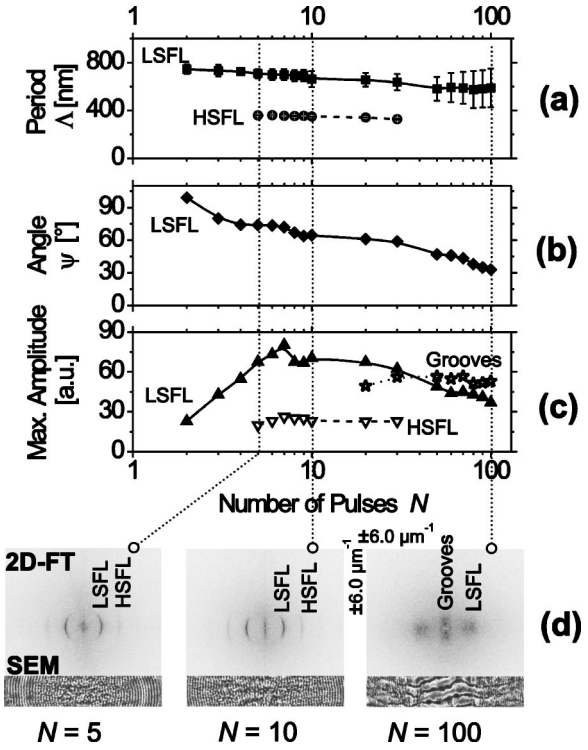

FIG. 3. Evolution of (a) the lateral periods of the LSFL and HSFL ripples, (b) the opening angle ψ of the sickle-shaped LSFL feature in the 2D-FT, and (c) the maximum Fourier amplitudes of both ripple-types as a function of the pulse number per spot ($\phi_0 = 0.58$ J/cm^2, 800 nm, 130 fs). Typical examples of the 2D-FTs used for evaluation and parts of the corresponding SEM images are displayed in (d). The dimension of the long axis of the SEM images is 41.3 μm. In (d), the Fourier amplitudes are encoded in a linear gray scale, with the dark regions representing the high values.

value broadens, as indicated by the error bars, i.e., ripples of various spatial periods around the average period are formed at the surface. Interestingly, in a very small pulse number range ($N = 5-30$), HSFL with periods Λ decreasing from 360 to 330 nm were found having nearly half of the spatial period of the LSFL and only a small variation around the average value [see the full circles in Fig. 3(a)]. This indicates that the formation of the HSFL is directly related to that of the LSFL. The coexistence of both types of ripples can be seen in the SEM images of Fig. 4. It has to be pointed out that this type of HSFL with periods of $\lambda/2-\lambda/3$ found after *above*-band-gap-excitation is significantly different from that observed by Borowiec and Haugen, where HSFL with lateral periods of $\lambda/4-\lambda/5$ were found solely for *below*-band-gap-excitation wavelength.[14]

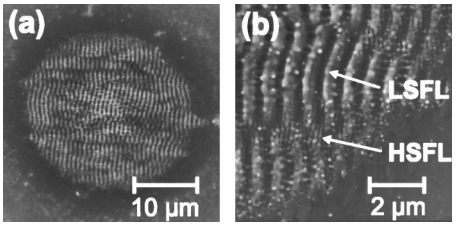

FIG. 4. SEM images of a surface region irradiated by ten subsequent laser pulses ($N = 10$, $\phi_0 = 0.24$ J/cm^2, 800 nm, 130 fs); (a) overview, (b) detail. The LSFL and HSFL rippled regions are marked by arrows in (b).

A more significant change can be observed in the evolution of the opening angle ψ as a function of the number of laser pulses [Fig. 3(b)]. For the LSFL, this angle strongly decreases from values around 100° ($N = 2$) to values around 30° for 100 pulses per spot, which indicates that the initially curved ripples develop into a pattern of more straight lines (a value of $\psi = 360°$ corresponds to a periodic pattern of equidistant circles having the same origin, whereas a perfect grating formed by parallel lines is represented by $\psi = 0°$). This is an additional indicator for the polarization-sensitive feedback mechanism involved in the ripple formation process.

Initially, the maximum amplitude of LSFL in the Fourier space grows logarithmically with the number of laser pulses as it can be seen as a straight line in the semilogarithmic representation in Fig. 3(c) for pulse numbers N between 1 and 7. This characteristic scaling behavior can be attributed to the increase in the ablated area in which the ripples are formed. In a previous study it has been shown that in InP, irradiated under similar experimental conditions ($\phi_0 = 0.58$ J/cm^2, $N = 100$), the ablated area also increases logarithmically with N which is a consequence of damage accumulation effects.[11] After reaching a nearly constant value ($N = 8-20$), the Fourier amplitudes fall off again when the LSFL peak starts to blur out ($N > 20-30$). Simultaneously, at those high pulse numbers, a characteristic pattern of grooves which is perpendicular to the ripple structures starts to develop from the center of the irradiated regions [see the star-shaped symbols in Fig. 3(c)]. Its spatial period is between 2 and 4 μm, which is more than 3 times larger than the LSFL period. The amplitudes of the HSFL feature are by far smaller than that of the LSFL and it shows only a weak dependence on the laser pulse number, peaked at around $N = 7$, as in case of the LSFL.

The two observations of (i) a lateral period of the HSFL which is half of that of the LSFL and (ii) the occurrence of the HSFL in the pulse number window where the LSFL are most pronounced both suggest that the HSFL are created by a nonlinear response of the surface structured with the LSFL, i.e., the involvement of a second-harmonic generation (SHG) at the rough surface. The initial growth phase of the LSFL leads to a significant surface roughening and near-surface material modification which allows the SHG process to occur. It should be mentioned that SHG is forbidden for normal incident radiation on a bulk zinc-blende semiconductor with (100) orientation.[21] Nevertheless, the nonlinear response of these materials is quite high[22] and there can be contributions due to surface SHG.[23] Moreover, by probing a rippled surface region (generated with five pulses at the same experimental conditions as the spot shown in Fig. 4) by micro-Raman spectroscopy over a depth of ~45 nm, it has been shown that besides a superficial amorphization, a polycrystalline reordering of the laser-induced resolidified melt layer underneath can also lead to crystallites with sizes between 100 and 500 nm and different orientations than the single-crystalline wafer material.[17] Such recrystallization phenomena can also lead to local contributions of the SHG. A similar conclusion has been drawn by Borowiec and Haugen, who observed an insensitivity of the HSFL to the crystal orientation and attributed that to the near-surface modifica-

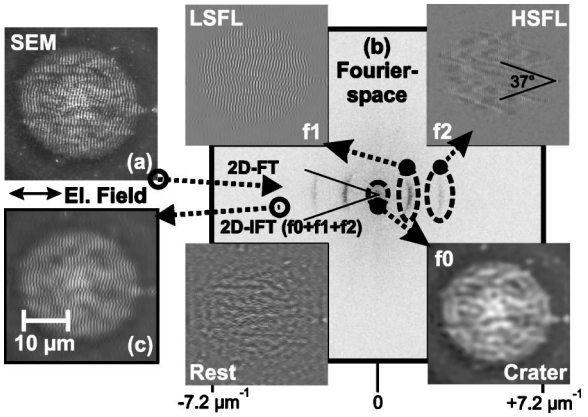

FIG. 5. Fourier analysis of a SEM image (a) of a surface region irradiated by ten subsequent laser pulses ($N=10, \phi_0=0.24$ J/cm^2, 800 nm, 130 fs). In (b), the Fourier amplitudes are encoded in a linear gray scale, with the dark regions representing the high values.

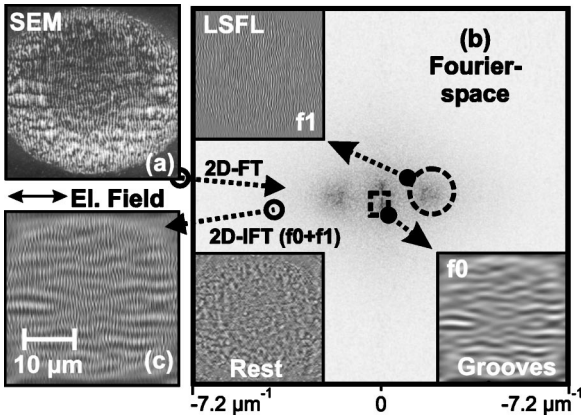

FIG. 6. Fourier analysis of a SEM image (a) of a surface region irradiated by 100 subsequent laser pulses ($N=100, \phi_0=0.24$ J/cm^2, 800 nm, 130 fs). Note that the Fourier amplitudes in (b) are encoded in the same gray scale used in Fig. 5(b).

tions upon multiple-pulse irradiation which might facilitate the harmonic generation.[14] On the other hand, for the higher pulse numbers, the surface starts to degrade by changes in the chemical composition or by further modification of the crystalline structure on a depth scale comparable to the penetration depth of the incident radiation. Along with the broader distribution of the LSFL periods, this material degradation finally leads to the disappearance of the HSFL.

In order to separate the different contributions to the surface topographies, some SEM images of typical irradiation spots were subjected to a 2D-FT and a subsequent retransformation of its most characteristic features which are contained in the Fourier space. Figure 5 shows an overview of the results obtained by this procedure. In Fig. 5(a), the original SEM image is given. For the given pulse number ($N=10$), at a fluence close to the single-pulse ablation threshold, three characteristic features can be seen in the Fourier space [Fig. 5(b)], which are marked with dashed lines. Each of those regions have then been retransformed separately via a two-dimensional inverse Fourier transformation (2D-IFT), whose results are displayed as insets f0–f2. The dominant sickle-shaped feature in the Fourier space represents the LSFL [Fig. 5(b), f1] which cover the entire ablated area. The second sickle-shaped feature contains the topographical information of the HSFLs [Fig. 5(b), f2]. Interestingly, these ripples with nearly half-wavelength period show a distinct modulation pattern of the Fourier amplitudes such that the regions of locally increased amplitude values are arranged mainly on lines which intersect at angles of $(37\pm5)°$ [see the black lines in Fig. 5(b), f2]. This angle (37°) coincides within the experimental uncertainty with the opening angle of the sickle-shaped HSFL feature [see the black lines in Fig. 5(b)]. The central-circular shaped peak in the Fourier space represents, as already noted, the large-scale corrugations as the crater itself [Fig. 5(b), f0]. Retransforming the entire 2D-FT image excluding the three marked regions leads to an unspecific topography image [Fig. 5(b), inset "Rest"] which contains the residual image information on particles (debris) and other irregularities. In contrast, the inverse transformation of the combined three Fourier features, f0, f1, and f2, leads to the image shown in Fig. 5(c), which reproduces all essential information contained in the original SEM image.

C. Groove formation

A similar Fourier analysis of a crater region irradiated at the same fluence but with a ten times higher number of pulses per spot indicates a significantly different behavior, as is shown in Fig. 6. The SEM image (a) shows a surface region ablated with 100 subsequent pulses which is covered with both ripples and superimposed grooves on the crater walls and at its bottom. Interestingly, the grooves are arranged in a large-scale wavelike pattern with an orientation perpendicular to that of the ripples. The 2D-FT [Fig. 6(b)] indicates two characteristic regions, i.e., a blurred LSFL peak (marked by a dashed circle) and a large-scale corrugation region close to the origin of the image (marked by a dashed square). From the blurred nature of the peak it can be concluded that the ripples have a broad distribution of spatial periods, consistent with the error bars in the curve (squares) shown in Fig. 3(a). The retransformation of this feature leads to the image displayed in the corresponding inset f1, representing the LSFL. A retransformation of the second feature reveals that this part of the Fourier space contains the image information of the wavelike grooves [Fig. 6(b), inset f0]. The combined retransformation of the two marked regions (f0, and f1) reproduces well all the significant structures of the original SEM image [i.e., the crater, the LSFL, and the grooves; see Fig. 6(c)], whereas their exclusion in the 2D-IFT shows the rest of the surface structures which is not contained in these two areas of the Fourier space.

At this fluence of 0.24 J/cm^2, the grooves are less pronounced than in the case of 0.58 J/cm^2 [see the SEM for $N=100$ in Fig. 3(d)] indicating that this phenomenon depends—like the ripple formation—strongly on the laser fluence.

D. Comparison with the conventional theory on LIPSS

The currently most widely accepted theory of LIPSS is based on the interference of the incident laser beam with

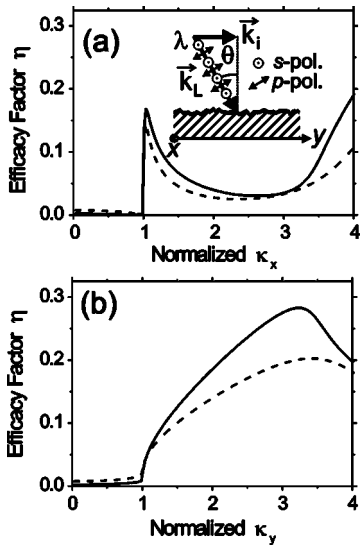

FIG. 7. Efficacy factor η as a function of the normalized LIPSS wave vector for (a) the direction parallel (κ_x) to the polarization vector and (b) perpendicular (κ_y) to it. In both cases η has been calculated for *s*-polarized light according to Eqs. (1)–(14) for normal incident radiation ($\theta=0$) and surface roughness parameters $s=0.4$ and $f=0.1$). The solid lines represent the results for *c*-InP [$\varepsilon(c\text{-InP},800\text{ nm})=(3.5+i0.2)^2$, Ref. 18], whereas the dashed lines show the results for *a*-InP [$\varepsilon(a\text{-InP},800\text{ nm})=(3.8+i0.5)^2$, Ref. 19]. The inset in (a) shows the general geometry of the rough surface irradiated with *s*- or *p*-polarized light (wavelength λ, wave vector $\mathbf{k}_L$, and angle of incidence θ).

some form of a surface-scattered electromagnetic wave. This fundamental idea has been first suggested by Emmony *et al.*[5] and was later improved by several other authors.[4,6] Particularly, the work of Sipe *et al.*[4] represents a first-principle theory which takes into consideration the interaction of an electromagnetic wave with a microscopically rough surface, which includes also the possible excitation of surface polaritons. This theory predicts possible LIPSS wave vectors $\mathbf{k}$ of the surface [with $|\mathbf{k}|=(2\pi)/\Lambda$] as a function of the laser parameters (angle of incidence θ, polarization direction, and wave vector of the incident radiation $\mathbf{k}_L$ [with $|\mathbf{k}_L|=(2\pi)/\lambda$] which has a component $\mathbf{k}_i$ in the surface plane [see the inset in Fig. 7(a)]) and surface parameters (dielectric constant and surface roughness). It leads to an expression for the inhomogeneous energy deposition into the irradiated material which is proportional to $\eta(\mathbf{k},\mathbf{k}_i)\times|b(\mathbf{k})|$, where η is a response function describing the efficacy with which the surface roughness at $\mathbf{k}$ leads to inhomogeneous absorption of radiation. The second factor b represents a measure of amplitude of the surface roughness at $\mathbf{k}$ which is a slowly varying function for a surface with a homogeneously distributed roughness.[4] In contrast to the behavior of b, the efficacy factor η can exhibit sharp peaks at certain $\mathbf{k}$ values which then determine the spatial ripple periods. It has to be noted here that once the LIPSS are formed, the Fourier spectrum of the surface $b(\mathbf{k})$ can also exhibit sharp peaks coincident with the peaks in $\eta(\mathbf{k})$ which were initially responsible for the surface damage. As already noted by Sipe *et al.*, the combined action of both functions makes the effect of surface rippling much more efficient due to the redistribution of the energy from subsequent laser pulses, i.e., feedback can occur. In later publications, Young and co-workers as well as Clark and Emmony have applied this first-principle theory to explain the formation of LIPSS in semiconductors[24–26] and metals[24,26] by analyzing quantitatively the efficacy factor $\eta(\mathbf{k},\mathbf{k}_i)$ for the given irradiation conditions.

Following this idea, the next paragraph will briefly summarize the mathematical definitions needed to calculate the efficacy factor on the basis of the mentioned first-principle theory of Sipe *et al.*.[4] It will use the general expressions given in that reference in order to get simplified equations for practical use in the present situation.

In the theory of Sipe *et al.*,[4] the efficacy factor is defined as

$$\eta(\mathbf{k},\mathbf{k}_i)=2\pi\left|v(\mathbf{k}_+)+v^*(\mathbf{k}_-)\right|. \tag{1}$$

For the two cases of *s*- or *p*-polarized light, incident under an angle of θ and having polarization vectors and a wave vector component $\mathbf{k}_i$ as shown in the inset of Fig. 7(a), the complex function v is given by

$$v(\mathbf{k}_\pm,s\text{-pol.})=[h_{ss}(k_\pm)(\hat{\mathbf{k}}_\pm\cdot\hat{\mathbf{y}})^2+h_{kk}(k_\pm)\times(\hat{\mathbf{k}}_\pm\cdot\hat{\mathbf{x}})^2]\gamma_t|t_s(\mathbf{k}_i)|^2, \quad \text{or} \tag{2a}$$

$$\begin{aligned}v(\mathbf{k}_\pm,p\text{-pol.})=&[h_{ss}(k_\pm)(\hat{\mathbf{k}}_\pm\cdot\hat{\mathbf{x}})^2+h_{kk}(k_\pm)\\&\times(\hat{\mathbf{k}}_\pm\cdot\hat{\mathbf{y}})^2]\gamma_t|t_x(\mathbf{k}_i)|^2+h_{kz}(k_\pm)\\&\times(\hat{\mathbf{k}}_\pm\cdot\hat{\mathbf{y}})\gamma_z\varepsilon t_x^*(\mathbf{k}_i)t_z(\mathbf{k}_i)+h_{zk}(k_\pm)\\&\times(\hat{\mathbf{k}}_\pm\cdot\hat{\mathbf{y}})\gamma_t t_x(\mathbf{k}_i)t_z^*(\mathbf{k}_i)\\&+h_{zz}(k_\pm)\gamma_z\varepsilon|t_z(\mathbf{k}_i)|^2,\end{aligned} \tag{2b}$$

with the inner products

$$(\hat{\mathbf{k}}_\pm\cdot\hat{\mathbf{y}})=(\sin\theta\pm\kappa_y)/\kappa_\pm \tag{3}$$

and

$$(\hat{\mathbf{k}}_\pm\cdot\hat{\mathbf{x}})=\kappa_x/\kappa_\pm. \tag{4}$$

Here, the definition $\kappa_\pm=\sqrt{\kappa_x^2+(\sin\theta\pm\kappa_y)^2}$ has been used and all lengths have been normalized with the factor $\lambda/(2\pi)$. Hence, the dimensionless LIPSS wave vectors $\kappa=k\times\lambda/(2\pi)\equiv\lambda/\Lambda$ are used in the following. With these definitions and with ε being the complex dielectric function of the material at the irradiation wavelength, the functions h_{ss}, h_{kk}, h_{kz}, h_{zk}, and h_{zz} used in Eqs. (2a) and (2b) can be expressed as

$$h_{ss}(\kappa_\pm)=\frac{2i}{\sqrt{1-\kappa_\pm^2}+\sqrt{\varepsilon-\kappa_\pm^2}}, \tag{5}$$

$$h_{kk}(\kappa_\pm)=\frac{2i\sqrt{(\varepsilon-\kappa_\pm^2)(1-\kappa_\pm^2)}}{\varepsilon\sqrt{1-\kappa_\pm^2}+\sqrt{\varepsilon-\kappa_\pm^2}}, \tag{6}$$

$$h_{kz}(\kappa_\pm)=\frac{2i\kappa_\pm\sqrt{\varepsilon-\kappa_\pm^2}}{\varepsilon\sqrt{1-\kappa_\pm^2}+\sqrt{\varepsilon-\kappa_\pm^2}}, \tag{7}$$

$$h_{zk}(\kappa_\pm) = \frac{2i\kappa_\pm\sqrt{1-\kappa_\pm^2}}{\varepsilon\sqrt{1-\kappa_\pm^2}+\sqrt{\varepsilon-\kappa_\pm^2}}, \tag{8}$$

and

$$h_{zz}(\kappa_\pm) = \frac{2i\kappa_\pm^2}{\varepsilon\sqrt{1-\kappa_\pm^2}+\sqrt{\varepsilon-\kappa_\pm^2}}. \tag{9}$$

Moreover, the complex functions t_s, t_x, and t_z are given by

$$t_s(\mathbf{k}_i) = \frac{2|\cos\theta|}{|\cos\theta|+\sqrt{\varepsilon-(\sin\theta)^2}}, \tag{10}$$

$$t_x(\mathbf{k}_i) = \frac{2\sqrt{\varepsilon-(\sin\theta)^2}}{\varepsilon|\cos\theta|+\sqrt{\varepsilon-(\sin\theta)^2}} \tag{11}$$

and

$$t_z(\mathbf{k}_i) = \frac{2\sin\theta}{\varepsilon|\cos\theta|+\sqrt{\varepsilon-(\sin\theta)^2}}. \tag{12}$$

The surface roughness is included in the theory in the factors γ_t and γ_z via two numerical factors, s (shape factor) and f (filling factor), by

$$\gamma_t = \frac{\varepsilon-1}{4\pi\left\{1+\left(\frac{1}{2}\right)(1-f)(\varepsilon-1)[F(s)-R\times G(s)]\right\}},$$

and

$$\gamma_z = \frac{\varepsilon-1}{4\pi\{\varepsilon-(1-f)(\varepsilon-1)[F(s)+R\times G(s)]\}},$$

with $R=(\varepsilon-1)/(\varepsilon+1)$ and the scalar functions

$$F(s) = \sqrt{s^2+1}-s, \tag{13}$$

and

$$G(s) = \left(\frac{1}{2}\right)(\sqrt{s^2+4}+s)-\sqrt{s^2+1}. \tag{14}$$

On the basis of Eqs. (1)–(14) it is possible to calculate numerically the efficacy factor η as a function of the normalized LIPSS wave vector components κ_x, κ_y at given values for the irradiation parameters (θ, λ, and polarization direction) and for parameters characterizing the optical (ε) and the surface roughness properties (s and f).

In order to compare our experimental results with predictions of the theory, we calculated the efficacy factor for s-polarized radiation (λ=800 nm) incident in normal direction (θ=0) onto single-crystalline indium phosphide [dielectric constant[18] $\varepsilon(c\text{-InP})=(3.5+i0.2)^2$] for the directions parallel (x) and perpendicular (y) to the polarization vector. Note in the following discussions that for LIPSS consisting of periodic lines being oriented in the direction perpendicular to the polarization vector, their grating (wave) vector $\boldsymbol{\kappa}$ is parallel to the polarization, which is here chosen to coincide with the x direction.

Following Refs. 4 and 24, the surface roughness was modeled with the values $s=0.4$ and $f=0.1$, which represent the assumption of spherically shaped islands. The results of the calculations are shown in Fig. 7 for the two directions parallel [Fig. 7(a), solid line] and perpendicular to the polarization vector [Fig. 7(b), solid line]. Since it is known that for fluences close to the ablation threshold an amorphous top layer can be formed on the InP surface, additionally the corresponding curves for bulk amorphous indium phosphide [dielectric constant[19] $\varepsilon(a\text{-InP})=(3.8+i0.5)^2$] are drawn in the same graphs with dashed lines.

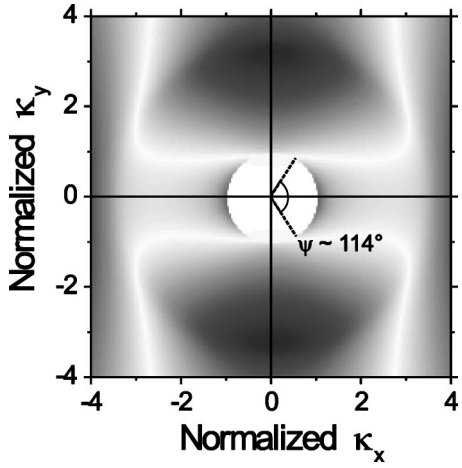

FIG. 8. Two-dimensional gray scale map of the efficacy factor η for c-InP as a function of the normalized LIPSS wave vector (the same parameters as in Fig. 7 have been chosen). High values of η are encoded in a linear gray scale with dark colors (range: $\eta\in[0,0.3]$). The cross section along the κ_x axis with $\kappa_x>0$ corresponds to the profile given in Fig. 7(a) and the cross section along the κ_y axis with $\kappa_y>0$ corresponds to the profile given in Fig. 7(b).

For the direction parallel to the polarization vector [Fig. 7(a)], a peak is found which starts to increase very sharply at $\kappa_x=1$ (i.e., $\Lambda=\lambda$) and which asymmetrically broadens towards higher κ_x values. Corresponding lateral ripple periods between 800 and ~600 nm are found within its full width at half maximum ($\Delta\kappa_x\sim0.34$), which is fully consistent with the observations from Fig. 3(a). For the direction perpendicular to the polarization vector [Fig. 7(b)] no sharp peaks but broad bands with a maximum around $\kappa_y=3.0-3.5$ are observed which would correspond to a wide distribution of ripple periods around ~250 nm (experimentally not observed). For both the crystalline and the amorphous phases the behavior is very similar, even if the amplitudes in η are somewhat higher in c-InP [Figs. 7(a) and 7(b)] and the broad band is shifted slightly towards higher κ_y values for a-InP [Fig. 7(b)]. The sharp peak in η for the direction parallel to the polarization clearly can be associated with the LSFL since (i) the spatial periods between 600 and 800 nm and (ii) the ripple orientation [see Fig. 5(a)] are well reproduced by the theory.

In order to compare these findings more quantitatively with the 2D-FT images obtained from the experimental SFM and SEM data, simulations have been performed in the entire $\kappa_x-\kappa_y$ plane for the 800-nm radiation incident onto a c-InP surface in normal direction. Figure 8 shows the corresponding linear gray-scale encoding of η in a LIPSS wave vector range identical to that of Fig. 2 and using the same numerical parameters as in Fig. 7.

Consistent with the experimental data, the theory predicts the sickle-shaped features (LSFL) which are formed for

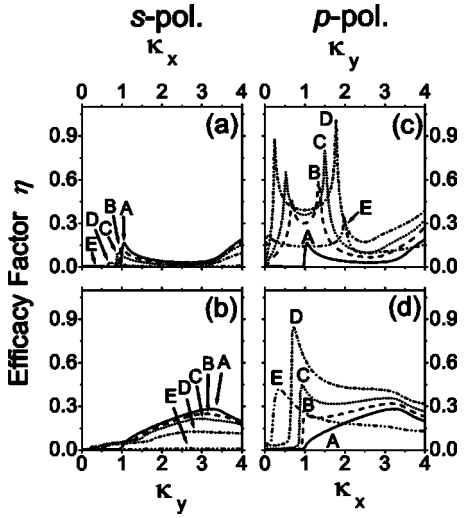

FIG. 9. Efficacy factor η for *c*-InP as a function of the normalized LIPSS wave vector for varying angles of incidence [curves A: $\theta=0°$ (solid), B: $\theta=20°$ (dashed), C: $\theta=30°$ (dotted), D: $\theta=50°$ (dash-dot), and E: $\theta=80°$ (dash-dot-dot)] and different polarization orientations. In (a) and (b), η is calculated for *s*-polarized radiation, whereas in (c) and (d) it is evaluated for *p*-polarized light. [Parameters: $s=0.4$ and $f=0.1$, $\varepsilon(c\text{-InP}, 800\ \text{nm})=(3.5+i0.2)^2$, Ref. 18]. Note that the curves in (a) and (c) represent sections along the direction parallel to the projection of the electric-field vector onto the surface, whereas the curves in (b) and (d) show the direction perpendicular to it.

$\kappa_x \sim \pm 1$ ($\Lambda \approx \lambda$). An opening angle of $\psi \sim 114°$ is found for this feature which deviates by only ~14% from the experimentally observed value for the interaction of the *second* laser pulse with the surface roughened by the first pulse [see Figs. 2(b) and 3(b) for $N=2$]. Nevertheless, it has to be noted here that a direct comparison of this angle with the experimental results is difficult, since in Fig. 8 the efficacy factor η is evaluated for a nonrippled surface, whereas in Figs. 2 and 3 the Fourier spectra b of the already rippled surfaces are displayed. Since the obviously acting feedback mechanism is not considered by the theory, this might explain the observed difference in the value of ψ. The calculations (not given here) also show that for *c*-InP under normal incident radiation the peak position of the efficacy factor is almost independent of the value of the filling factor f and the shape factor s, which means that the final LSFL are rather insensitive to the original surface morphology.

It is also evident from Fig. 8 that the HSFL features ($\kappa_x \sim \pm 2$, i.e., $\Lambda \approx \lambda/2$) are not described by the theory. This is an additional indicator for the nonlinear interaction mechanism proposed, since those effects are not included in the theory which was used. Since also the formation of a crater is not included in the framework of the LIPSS theory, the central structures in the 2D-FT images of Figs. 2, 5, and 6 cannot be reproduced.

More detailed simulations for *c*-InP with varying angles of incidence for *s*- and *p*-polarized radiation (Fig. 9) reveal some additional interesting aspects: the theory [Eqs. (1)–(14)] then predicts different peak amplitudes for the maximum in η (LSFL peak) for *s*-polarized [Figs. 9(a) and 9(b)] and for *p*-polarized [Figs. 9(c) and 9(d)] radiation. Note that the curves shown in (a) and (c) represent evaluations of η for the direction parallel to the projection of the electric-field vector to the surface (i.e., the direction perpendicular to the lines of the ripples), whereas the results given in (b) and (d) are calculations for the direction perpendicular to it (i.e., the direction perpendicular to the lines of the grooves). Consistent, with the vanishing difference between *s*- and *p*-polarization for normal incident radiation, the curves for $\theta=0°$ (labeled with an A) are identical in (a) and (c), as well as in (b) and (d). For increasing angles of incidence (curves B: $\theta=20°$, C: $\theta=30°$, D: $\theta=50°$, and E: $\theta=80°$), the LSFL peak for the *p*-polarization direction splits into a double-peak structure with the dominant maximum shifting towards the larger κ values (but limited to the range $\kappa \leqslant 2$) and the less dominant peak shifting towards the smaller values [see Fig. 9(c)]. Along with this shift, the peak value of the absolute maximum first increases and then decreases again. In the *s*-polarization direction, however, the LSFL peak does not split, but shifts towards a smaller value and decreases in amplitude [see Fig. 9(a)]. Since in the experimental situation of a linearly polarized beam focused on the sample surface, some nonnormal contributions of both polarization directions may always be expected, and due to local changes of the angle of incidence upon the formation of the crater at the surface, the observed LSFL may be attributed to the dominant *p*-polarization component of the incident radiation. In addition, the decrease in the average LSFL period with the pulse number as seen in Fig. 3(a) can then be affected by the rising angle of incidence upon the formation of a crater with increasing depth.

Furthermore, it has to be noted that the theory for normal incident radiation does not predict an increased light absorption at the spatial frequencies of the groove structures observed in the experiments [see Figs. 3(d) and 6(a)]. The calculations shown in Fig. 9 indicate that, in order to explain a peak in η perpendicular to the polarization vector and with spatial periods between 2 and 4 μm ($|\kappa_y| \sim 1/3-1/5$), angles of incidence larger than $\theta \sim 80°$ would be necessary [see curves E for *p*-polarized radiation in Fig. 9, where the peak in that wave-number region in (d) exhibits a higher amplitude than the corresponding peaks in (c)] which can only be realized if a reflection at the crater wall towards its center is involved once a critical crater depth is exceeded. Note that the sharp peaks in η for $\kappa_y < 1$ in Fig. 9(c) cannot be responsible for the groove formation process since the direction of those periodic structures would be perpendicular to the experimentally observed orientation of the grooves.

In summary, the conventional LIPSS theory accurately describes the observed LSFL but is not able to describe the HSFL and the groove structures. However, by this work we hope to stimulate further studies on the formation of femtosecond LIPSS, especially with respect to the extension of the existing first-principle theory, which could include nonlinear effects and which should throw light on the groove formation mechanisms.

IV. CONCLUSIONS

Single-crystalline InP was exposed in air to single and multiple Ti:sapphire femtosecond laser pulses (800 nm, 130 fs) at fluences above the single-pulse ablation threshold

$[>\phi_{abl}(1)=0.23\ J/cm^2]$. The resulting ablative formation of craters and laser-induced periodic surface structures (LIPSS; ripples) on InP was investigated in detail by means of scanning force microscopy (SFM) and scanning electron microscopy (SEM). The observed topographic structures were analyzed using two-dimensional Fourier transformation (2D-FT) analysis. Depending on the number of laser pulses applied to the same spot, two different types of ripples could be distinguished which change their characteristic parameters upon this variation, i.e., the lateral period, their curvature, and their size distribution. In all cases their orientation was perpendicular to the electric-field vector. Nearly wavelength-sized ripples [low-spatial-frequency LIPSS (LSFL)] were already present after the second pulse, but were never observed for single-pulse irradiation. This indicates that the first pulse is needed to generate a rough surface exhibiting topographical structures with sizes in the order of the laser wavelength. These structures are reinforced by the subsequent laser pulses via a feedback mechanism based on the interference of the incident radiation with a surface electromagnetic wave. The spatial period of the LSFL decreases from 750 nm ($N=2$) to 590 nm ($N=100$) which can be explained by the locally increasing angle of incidence upon the formation of a crater. Along with this, the LSFL orientation develops from significantly curved (2D-FT: $\psi\sim 100°$ for $N=2$) to straighter lines (2D-FT: $\psi\sim 30°$ for $N=100$). After 4–5 pulses per spot, the LSFL ripples are most pronounced and generate additional ripples via the second-harmonic generation (SHG). These additional ripples [high-spatial-frequency LIPSS (HSFL)] exhibit a lateral period half of that of the LSFL. For pulse numbers higher than 20, the spatial distribution of the LSFL significantly broadens and the Fourier amplitudes decrease simultaneously. As a consequence the HSFL disappear also, which is attributed to the chemical or structural changes of the surface in the irradiated areas. For $N>50$, characteristic groove structures with periods between 2 and 4 μm are formed which are oriented perpendicular to the LSFL. A quantitative comparison with the currently accepted LIPSS theory confirms that the LSFL features can be properly described within its framework, whereas the HSFL and the groove structures are not included in it.

ACKNOWLEDGMENTS

The authors would like to thank B. Strauß and S. Benemann (BAM, Laboratory VIII.23: Surface and Thin Film Analysis) for the SEM investigations and Professor J. M. Wrobel (University of Missouri-Kansas City) for his courtesy of providing the InP wafers. One of the authors (J.B.) acknowledges the funding of the C.S.I.C. through a contract in the frame of the I3P program (Ref. I3P-PC2002), co-funded by the European Social Fund.

[1] M. Birnbaum, J. Appl. Phys. **36**, 3688 (1965).
[2] H. M. van Driel, J. E. Sipe, and J. F. Young, Phys. Rev. Lett. **49**, 1955 (1982).
[3] A. E. Siegman and P. M. Fauchet, IEEE J. Quantum Electron. **QE-22**, 1384 (1986), and references therein.
[4] J. E. Sipe, J. F. Young, J. S. Preston, and H. M. van Driel, Phys. Rev. B **27**, 1141 (1983).
[5] D. C. Emmony, R. P. Howson, and L. J. Willis, Appl. Phys. Lett. **23**, 598 (1973).
[6] Z. Guosheng, P. M. Fauchet, and A. E. Siegman, Phys. Rev. B **26**, 5366 (1982).
[7] J. Krüger, Ph.D. thesis, BTU Cottbus, 1999.
[8] J. Bonse, H. Sturm, D. Schmidt, and W. Kautek, Appl. Phys. A: Mater. Sci. Process. **71**, 657 (2000).
[9] G. Dumitru, V. Romano, H. P. Weber, M. Sentis, and W. Marine, Appl. Surf. Sci. **205**, 85 (2003).
[10] J. Bonse, S. Baudach, J. Krüger, W. Kautek, and M. Lenzner, Appl. Phys. A: Mater. Sci. Process. **74**, 19 (2002).
[11] J. Bonse, J. M. Wrobel, J. Krüger, and W. Kautek, Appl. Phys. A: Mater. Sci. Process. **72**, 89 (2001).
[12] A. Borowiec, M. Couillard, G. A. Button, and H. K. Haugen, Appl. Phys. A: Mater. Sci. Process. **79**, 1887 (2004).
[13] F. Costache, S. Kouteva-Arguirova, and J. Reif, Appl. Phys. A: Mater. Sci. Process. **79**, 1429 (2004).
[14] A. Borowiec and H. K. Haugen, Appl. Phys. Lett. **82**, 4462 (2003).
[15] N. Yasumaru, K. Myazaki, and J. Kiuchi, Appl. Phys. A: Mater. Sci. Process. **76**, 983 (2003).
[16] J. Bonse, J. M. Wrobel, K.-W. Brzezinka, N. Esser, and W. Kautek, Appl. Surf. Sci. **202**, 272 (2002).
[17] J. Bonse, M. Munz, and H. Sturm, IEEE Trans. Nanotechnol. **3**, 358 (2004).
[18] O. J. Glembocki and H. Piller, in *Handbook of Optical Constants of Solids*, edited by E. D. Palik (Academic, Orlando, 1998).
[19] J. Stuke and G. Zimmerer, Phys. Status Solidi B **49**, 587 (1985).
[20] V. I. Emel'yanov and D. V. Babak, Appl. Phys. A: Mater. Sci. Process. **74**, 797 (2002).
[21] S. Sauvage, Y. Bernard, I. Sagnes, G. Patriarche, F. Glas, G. Le Roux, M. Bensoussan, and J. A. Levenson, J. Opt. Soc. Am. B **18**, 81 (2001).
[22] S. Bergfeldt and W. Daum, Phys. Rev. Lett. **90**, 036801 (2003). At the given fundamental wavelength of 800 nm, values between 400 and 800 pm/V have been reported for the only six nonvanishing components $\chi^{(2)}_{xyz}$ of the second-order nonlinear susceptibility tensor of *c*-GaAs. B. Adolph and F. Bechstedt, Phys. Rev. B **57**, 6519 (1999). These values are ~3–4 times higher than that of *c*-InP having the same crystal symmetry.
[23] G. Lüpke, Surf. Sci. Rep. **35**, 75 (1999).
[24] J. F. Young, J. S. Preston, H. M. van Driel, and J. E. Sipe, Phys. Rev. B **27**, 1155 (1983).
[25] J. F. Young, J. E. Sipe, and H. M. van Driel, Phys. Rev. B **30**, 2001 (1984).
[26] S. E. Clark and D. C. Emmony, Phys. Rev. B **40**, 2031 (1989).